Extended Fourth-Order Depth-Integrated Model for Water Waves and Currents Generated by Submarine Landslides

Hongqiang Zhou[1] and Michelle H. Teng, M.ASCE[2]

Abstract: In this paper, a preexisting higher-order depth-integrated wave propagation model is extended to include a moving seabed. As a result, the extended model can be applied to both wave propagation and the dynamic process of wave generation by a seabed disturbance such as a submarine landslide. The model has the linear dispersion relation in a form of (4,4) Padè approximant, and approximates the water velocity profiles along the water depth with a fourth-order polynomial of the vertical coordinates. The fourth-order model is aimed at extending the validity of the lower-order depth-integrated models from long waves to both long and shorter waves, as well as improving the approximation of the velocity field from the second order to the fourth order. Laboratory experiments are carried out in a wave flume to study wave generation by a submerged landslide model. Both water waves and water velocities are measured by using resistance-type wave gauges and a particle image velocimetry. The experimental data are then compared with the predicted wave height and water current based on the new model and two existing lower-order Boussinesq-type models. The results clearly show that the new model predicts the fluid velocity more accurately and is also able to predict the shorter trailing waves very well where the traditional Boussinesq model may be inadequate, thus validating the improvement provided by the fourth-order model.

DOI: 10.1061/(ASCE)EM.1943-7889.0000087

CE Database subject headings: Water waves; Velocity; Landslides; Models.

Author keywords: Depth-integrated model; Water wave; Water velocity; Submarine landslide.

Introduction

Submarine landslide is a common cause to tsunamis. Tsunamis generated by submarine landslides may be as destructive as those generated by earthquakes especially near the source area and when the landslide involves large volumes of debris spreading over several kilometers. Most of the historical tsunamigenic submarine landslides happened on very mild slopes with slope angles less than 10°. The ratio of landslide thickness to its length and the ratio of submergence depth to landslide length were usually less than 0.1 (Hampton et al. 1996). The typical geological features of submarine landslides imply that the depth-integrated modeling approaches may be applied to predict the water waves and currents that the landslides generate. Compared with the three-dimensional (3D) models, depth-integrated models are easier to solve and are more efficient computationally.

In many of the existing studies, shallow-water equations (Jiang and LeBlond 1992, 1993; Rabinovich et al. 1999; Imran et al. 2001; Fine et al. 2003, 2005) were applied to simulate the landslide-generated tsunamis. In the shallow-water equations, the effects of frequency dispersion are neglected and the water velocities are assumed to be uniform along the water depth. These assumptions are valid only for landslides of very flat and thin shapes sliding down along extremely mild slopes in shallow water. To consider the weakly dispersive waves generated by a seabed disturbance, the Boussinesq models (Wu 1981; Villeneuve and Savage 1993) have also been developed. These models retain the lowest order of frequency dispersion, i.e., $O(\mu^2)$ where $\mu = h_0/\lambda_0$, with h_0 being the characteristic still-water depth and λ_0 the characteristic wavelength, and approximate the vertical profiles of water velocities with quadratic functions of the vertical coordinate. While these models are applicable to many real-world scenarios, in some other cases where the landslide is relatively short or the seabed has a steeper slope, the weakly dispersive assumptions may become insufficient.

To extend the applicability of the traditional Boussinesq model from long waves to shorter waves, Nwogu (1993) developed a new form of the Boussinesq model, in which the velocity at a reference water level z_α between the still-water surface and the sea bottom is used instead of the conventional depth-averaged velocity. It was shown that by defining the reference level at a particular depth, i.e., $z_\alpha \cong -0.531h$ where h is the still-water depth, the model by Nwogu (1993) can retain the appropriate linear dispersion relation for the wavelengths from very long to as short as $\lambda_0 = 2h_0$, which is an improvement over the traditional Boussinesq models. Wei et al. (1995) and Wei and Kirby (1995) extended the wave propagation model of Nwogu (1993) by considering the fully nonlinear effects. The fully nonlinear weakly dispersive Boussinesq-type model [of $O(\mu^2)$] was later further extended by Lynett and Liu (2002) by introducing movable seabed conditions, and Chen et al. (2003) by considering the vertical vorticity. By using the same idea of Nwogu (1993), multilayer

[1]NRC Research Associate, Pacific Marine Environmental Laboratory, National Oceanic and Atmospheric Administration, Seattle, WA 98115 (corresponding author). E-mail: hongqiang.zhou@noaa.gov

[2]Associate Professor, Dept. of Civil and Environmental Engineering, Univ. of Hawaii at Manoa, Honolulu, HI 96822. E-mail: teng@eng.hawaii.edu

Note. This manuscript was submitted on December 9, 2008; approved on September 4, 2009; published online on September 7, 2009. Discussion period open until September 1, 2010; separate discussions must be submitted for individual papers. This paper is part of the ***Journal of Engineering Mechanics***, Vol. 136, No. 4, April 1, 2010. ©ASCE, ISSN 0733-9399/2010/4-506–516/$25.00.

models have also been developed to obtain higher-order dispersion relation (Lynett and Liu 2004; Hsiao et al. 2005), or to simulate the flows inside and above a permeable seabed (Hsiao et al. 2002; Cruz and Chen 2007). These valuable contributions have greatly extended the applicability of the depth-integrated models to a much broader range of applications in coastal and hydraulic engineering. The research group led by Madsen also made significant contributions to the enhancement of the traditional Boussinesq models. For example, by rearranging the dispersive terms, Madsen et al. (1991), Madsen and Sørensen (1992), and Schäffer and Madsen (1995) were also able to enhance the dispersion relation of Boussinesq-type equations. In recent years, the development of computer technology has made it possible to apply the Boussinesq-type models in much larger scales (Løvholt et al. 2008; Geist et al. 2009).

Although the pioneering idea of Nwogu (1993) on using velocity at z_α improved the dispersion relation to cover a broader wavelength spectrum, the dispersion terms in his model are still at the same order as those in the traditional Boussinesq model. In the fully nonlinear fourth-order model equations of Gobbi and Kirby (1999) and Gobbi et al. (2000), a weight-averaged water velocity potential $\tilde{\phi}$ was defined to enhance the dispersion relation, i.e.

$$\tilde{\phi} = \gamma\phi_\alpha + (1-\gamma)\phi_\beta \tag{1}$$

where $\phi_\alpha = \phi(x,y,z_\alpha,t)$ and $\phi_\beta = \phi(x,y,z_\beta,t)$ = velocity potentials at water levels $z_\alpha = \alpha h$ and $z_\beta = \beta h$ and γ = weighting factor. In this model, the profiles of water velocity potential are approximated with a fourth-order polynomial of vertical coordinates.

Ataie-Ashtiani and Najafi-Jilani (2007) developed a new form of fully nonlinear higher-order dispersive model which assumes time-variable seafloor bathymetry. In this model, they defined a weight-averaged reference water level $\tilde{z}$ as follows:

$$\tilde{z} = \gamma z_\alpha + (1-\gamma) z_\beta \tag{2a}$$

$$\tilde{z}^n = \gamma z_\alpha^n + (1-\gamma) z_\beta^n \tag{2b}$$

where n indicates the "nth" power of $\tilde{z}$. The parameters γ, α, and β are the same as in the study of Gobbi and Kirby (1999). We note that the expression of $\tilde{z}^n$ in Eq. (2*b*) is mathematically inconsistent with the expression for $\tilde{z}$ in Eq. (2*a*), and therefore the validity of the final model equations is questionable. Furthermore, Fuhrman and Madsen (2009) have also raised questions about the numerical simulations in the paper by Ataie-Ashtiani and Najafi-Jilani (2007).

To further extend the applicability of Boussinesq-type models to even shorter waves, Agnon et al. (1999), Madsen et al. (2002, 2003, 2006), and Fuhrman and Madsen (2008, 2009) developed a higher-order Boussinesq-type model in which the linear dispersion relation is accurate to $kh \approx 25$ (or $\lambda_0 \approx 0.25h$), where $k = 2\pi/\lambda_0$ is the wave number. This model involves a truncated Taylor expansion of water velocity around a specified water level, and retains the vertical water velocity as an unknown. Their model also involves the assumption of mild sloping bathymetry to remove higher-order derivatives of water depth h. More recently, the new Boussinesq-type model is extended to consider water wave generation by time-variable bathymetry (Fuhrman and Madsen 2009).

Besides applying the depth-integrated models, researchers have also carried out excellent studies on landslide-generated waves by applying 3D models such as the potential theory (Grilli and Watts 1999, 2005; Grilli et al. 2002) or the *N-S* equations [Liu et al. (2005); Yuk et al. (2006), among others].

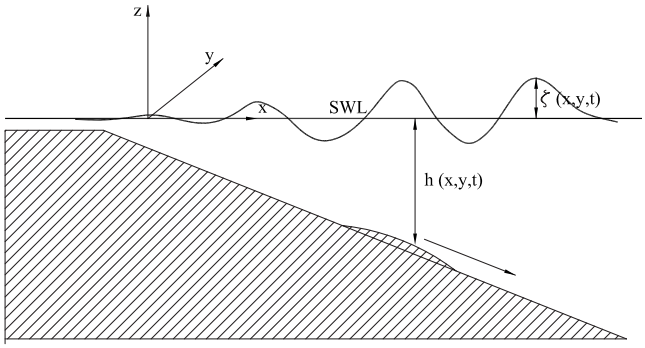

Fig. 1. Sketch of a submarine landslide and the water waves it generates

The focus of this study is to develop a depth-integrated higher-order model for predicting landslide-generated waves and currents. Specifically, we follow the sound modeling approach introduced by Gobbi and Kirby (1999) and Gobbi et al. (2000) to extend their earlier model by including the time-variable seabed condition induced by submerged moving disturbances. This extension enables the new model to be applicable to modeling both wave propagation and wave generation by submarine landslides. After the theoretical model is derived, a finite-difference scheme is constructed to solve the equations. In addition, a series of wave flume experiments are carried out to measure the wave heights and the water velocities generated by submerged moving landslide models. We note that in the recent decade, development of higher-order wave models has been very active. However, the validation of these models against laboratory experiments was not always reported. This is partly because most available data of existing experiments on landslide-generated waves are not applicable to the depth-integrated models since in these existing experiments, the landslide models were usually triangular or rectangular blocks whose sharp edges induce significant flow separation and secondary flows, or were initially submerged in much deep water depth. In addition, most of the existing experimental studies focused on the measurement of surface waves while the water velocities were seldom measured (e.g., Wiegel 1955; Watts 1998, 2000; Sue et al. 2006). In engineering applications, accurate prediction of water current in a tsunami is equally important as that of the wave height since current can also cause damaging impact on coastal structures such as scouring of the structural foundation. Therefore, there is a need for more experimental data for both the wave heights and the fluid velocities generated by submerged moving disturbances, so that researchers can use these data for better understanding of the wave mechanism and more complete validation of different wave models. The experimental data in this study are used to examine the validity of the new higher-order model as well as two existing lower-order models. The detailed results and discussions are presented in the following sections, including the explanation of the differences between the current model and those by Ataie-Ashtiani and Najafi-Jilani (2007) and Fuhrman and Madsen (2009).

Fourth-Order Model

Fig. 1 shows a schematic diagram of the physical problem of interest in this study. The origin of the Cartesian coordinate

system is set on the still-water level, with vertical coordinate z pointing upward. The water surface displacement is denoted by ζ and the water depth is h. The water depth below the still-water surface is assumed to be a function of both space and time, i.e., $h=h(x,y,t)$. The present study assumes incompressible and irrotational flows, and the governing equations are given by

$$\phi_{zz} + \mu^2 \nabla^2 \phi = 0, \quad -h \leq z \leq \varepsilon\zeta \tag{3}$$

$$\frac{\mu^2}{\varepsilon} h_t + \mu^2 \nabla \phi \cdot \nabla h + \phi_z = 0, \quad z = -h \tag{4}$$

$$\zeta_t + \varepsilon \nabla \phi \cdot \nabla \zeta - \frac{1}{\mu^2} \phi_z = 0, \quad z = \varepsilon\zeta \tag{5}$$

$$\zeta + p + \phi_t + \frac{1}{2}\varepsilon \left[\nabla\phi \cdot \nabla\phi + \frac{1}{\mu^2}(\phi_z)^2 \right] = 0, \quad z = \varepsilon\zeta \tag{6}$$

where ϕ=water velocity potential; $\nabla=(\partial/\partial x, \partial/\partial y)$=horizontal gradient operator; and p=atmospheric gauge pressure on the water surface. The above equations are in nondimensional form with the dimensional variables scaled in the following manner:

$$(x,y) = \frac{(x',y')}{\lambda_0}, \quad (z,h) = \frac{(z',h')}{h_0}, \quad t = \frac{\sqrt{gh_0}t'}{\lambda_0}$$

$$\zeta = \frac{\zeta'}{a_0}, \quad \phi = \frac{\phi'}{\varepsilon\lambda_0\sqrt{gh_0}}, \quad p = \frac{p'}{\rho g a_0} \tag{7}$$

where the primes denote the dimensional variables; parameter ε represents the effect of nonlinearity; and $\varepsilon=a_0/h_0$ where a_0 is the characteristic wave amplitude. In the present study, the gauge air pressure on the free surface is assumed to be zero.

From Eqs. (3)–(6), we can derive a new depth-integrated wave model, which retains the fully nonlinear terms and is truncated at $O(\mu^6)$ for frequency dispersion. The derivation follows closely the expansion method and steps by Gobbi and Kirby (1999) and Gobbi et al. (2000). The difference between the current model and the model by Gobbi and Kirby (1999) is that in the current study, we have included the time variation in water depth h. As a result, the present model can be applied to the wave generation by submerged moving objects, in addition to wave propagation over spatially variable depth as in Gobbi and Kirby (1999). For simplicity, the detailed derivation is omitted in this paper but can be found in Zhou (2008).

The present fully nonlinear and fourth-order dispersive model, which will be referred to as the $O(\mu^4)$-model thereafter in this paper, consists of two equations for two unknowns, namely, the water surface elevation ζ and weight-averaged velocity potential $\tilde{\phi}$, as defined in Eq. (1). Specifically, the first equation is the continuity equation given by

$$\frac{H_t}{\varepsilon} + \nabla \cdot \mathbf{Q} = O(\mu^6) \tag{8}$$

where $H=h+\varepsilon\zeta$=total water depth including the water surface displacement ζ, and

$$\begin{aligned}\mathbf{Q} = {} & H\nabla\tilde{\phi} + \mu^2 H\left\{\left[(A-1)F_1 + 2\left(Bh - \frac{H}{2}\right)F_2\right]\nabla h \right. \\ & \left. + \left(Ah - \frac{H}{2}\right)\nabla F_1 + \left(Bh^2 - \frac{H^2}{3}\right)\nabla F_2\right\} \\ & + \mu^4 H\left\{\left[(A-1)F_3 + 2\left(Bh - \frac{H}{2}\right)F_4 + 3\left(Ch^2 - \frac{H^2}{3}\right)F_5 \right.\right. \\ & \left.\left. + 4\left(Dh^3 - \frac{H^3}{4}\right)F_6\right]\nabla h + \left(Ah - \frac{H}{2}\right)\nabla F_3 \right. \\ & \left. + \left(Bh^2 - \frac{H^2}{3}\right)\nabla F_4 + \left(Ch^3 - \frac{H^3}{4}\right)\nabla F_5 + \left(Dh^4 - \frac{H^4}{5}\right)\nabla F_6\right\}\end{aligned}$$

in which

$$G = \frac{1}{1 + \mu^2 \nabla h \cdot \nabla h}$$

$$\tilde{S} = \nabla^2\tilde{\phi}, \quad \tilde{T} = \nabla h \cdot \nabla\tilde{\phi} + \frac{h_t}{\varepsilon}$$

$$F_1 = G\tilde{T}, \quad F_2 = \frac{1}{2}G\tilde{S}, \quad F_3 = \nabla h \cdot \nabla(Ah\tilde{T}) + \nabla h \cdot \nabla(Bh^2\tilde{S})$$

$$F_4 = \frac{1}{2}A\nabla^2(h\tilde{T}) + \frac{1}{4}B\nabla^2(h^2\tilde{S}) - \frac{1}{2}\nabla^2 h\tilde{T} - \nabla h \cdot \nabla\tilde{T}$$

$$F_5 = -\frac{1}{6}\nabla^2 h\tilde{S} - \frac{1}{3}\nabla h \cdot \nabla\tilde{S} - \frac{1}{6}\nabla^2\tilde{T}, \quad F_6 = -\frac{1}{24}\nabla^2\tilde{S}$$

$$A = \gamma(1+\alpha) + (1-\gamma)(1+\beta), \quad B = \gamma(1+\alpha)^2 + (1-\gamma)(1+\beta)^2$$

$$C = \gamma(1+\alpha)^3 + (1-\gamma)(1+\beta)^3, \quad D = \gamma(1+\alpha)^4 + (1-\gamma)(1+\beta)^4$$

The second equation is the approximate Euler equation

$$\begin{aligned}\zeta + \tilde{\phi}_t + \frac{1}{2}\varepsilon\nabla\tilde{\phi}\cdot\nabla\tilde{\phi} + \mu^2 I_2 + \mu^4 I_4 + \frac{1}{2}\varepsilon\mu^2(2\nabla\tilde{\phi}\cdot\mathbf{\Gamma}_2 + J_2^2) \\ + \frac{1}{2}\varepsilon\mu^4(\mathbf{\Gamma}_2\cdot\mathbf{\Gamma}_2 + 2\nabla\tilde{\phi}\cdot\mathbf{\Gamma}_4 + 2J_2J_4) = O(\mu^6)\end{aligned} \tag{9}$$

where

$$I_2 = [(A-1)F_1 + 2(Bh-H)F_2]h_t + (Ah-H)F_{1t} + (Bh^2-H^2)F_{2t}$$

$$\begin{aligned}I_4 = {} & [(A-1)F_3 + 2(Bh-H)F_4 + 3(Ch^2-H^2)F_5 \\ & + 4(Dh^3-H^3)F_6]h_t + (Ah-H)F_{3t} + (Bh^2-H^2)F_{4t} \\ & + (Ch^3-H^3)F_{5t} + (Dh^4-H^4)F_{6t}\end{aligned}$$

$$J_2 = -(F_1 + 2HF_2)$$

$$J_4 = -(F_3 + 2HF_4 + 3H^2F_5 + 4H^3F_6)$$

$$\begin{aligned}\mathbf{\Gamma}_2 = {} & [(A-1)F_1 + 2(Bh-H)F_2]\nabla h + (Ah-H)\nabla F_1 \\ & + (Bh^2-H^2)\nabla F_2\end{aligned}$$

$$\begin{aligned}\mathbf{\Gamma}_4 = {} & [(A-1)F_3 + 2(Bh-H)F_4 + 3(Ch^2-H^2)F_5 \\ & + 4(Dh^3-H^3)F_6]\nabla h + (Ah-H)\nabla F_3 + (Bh^2-H^2)\nabla F_4 \\ & + (Ch^3-H^3)\nabla F_5 + (Dh^4-H^4)\nabla F_6\end{aligned}$$

The determination of specific parameters α, β, and γ can be found in Gobbi and Kirby (1999) and Gobbi et al. (2000). In this study, these parameters are given by $\gamma=0.206$, $\alpha=-0.413$, and $\beta=-0.775$.

After ζ and $\tilde{\phi}$ are solved from Eqs. (8) and (9), the original velocity potential ϕ can be calculated by

$$\phi = \tilde{\phi} + \mu^2\{(Ah-\xi)F_1 + (Bh^2-\xi^2)F_2\} + \mu^4\{(Ah-\xi)F_3 + (Bh^2-\xi^2)F_4 + (Ch^3-\xi^3)F_5 + (Dh^4-\xi^4)F_6\} + O(\mu^6)$$

The fluid velocity components are then solved by $\mathbf{u}=\nabla\phi$ and $w=\partial\phi/\partial z$. We note that the vertical profile of horizontal fluid velocity $\mathbf{u}$ is a fourth-order function of z while that of the vertical component w is third-order in z. If there is no time variation in the still-water depth then the current wave model in Eqs. (8) and (9) becomes identical to that by Gobbi and Kirby (1999).

An important issue in deriving the fourth-order model is the determination of the optimal value of the weighing factor γ in Eq. (1). As shown by Gobbi and Kirby (1999) and Gobbi et al. (2000), the optimal value of γ was determined by making the fourth-order equations to satisfy the (4,4) Padè approximant to the analytical solution of the dispersion relation for linear periodic waves propagating over constant water depth. This approach has also been employed by other researchers to improve the linear dispersion relation of depth-integrated models (e.g., Nwogu 1993; Lynett and Liu 2004), partly because there are no analytical solutions available for waves propagating over arbitrarily varying water depth or for wave generation by external forcing. It is understandable that model parameters determined in this method do not automatically guarantee the model improvement for predicting wave generation and wave propagation over variable depth. This is the reason that validating the wave model against laboratory experiments or field data are extremely important. This is one of the objectives of the present study.

We would also like to discuss about the difference between the present fourth-order model and the models by Ataie-Ashtiani and Najafi-Jilani (2007) and Fuhrman and Madsen (2009). In principle, the present model and the model by Ataie-Ashtiani and Najafi-Jilani (2007) are fundamentally the same in that both are fully nonlinear and fourth order in dispersion, and both adopted many important results from the studies by Gobbi and Kirby (1999) and Gobbi et al. (2000). The main difference is that the current model involves two equations [Eqs. (8) and (9)] for two unknowns while the model by Ataie-Ashtiani and Najafi-Jilani (2007) involved three equations for three unknowns. In addition, as mentioned earlier, questions about the derivation and the numerical results in the paper of Ataie-Ashtiani and Najafi-Jilani (2007) remain to be resolved. The recent model derived by Fuhrman and Madsen (2009) is another higher-order model for wave propagation and wave generation. In the study of Fuhrman and Madsen (2009), the model was soundly derived and the numerical results were obtained carefully and correctly. On the other hand, since the wave model consists of a set of four equations for four unknowns, the current model may be simpler and easier to implement numerically.

We note that the present $O(\mu^4)$-model can be reduced to the fully nonlinear and weakly dispersive model of Lynett and Liu (2002), which will be referred to as the $O(\mu^2)$-model. In this case, Eqs. (8) and (9) are truncated at $O(\mu^4)$ and the velocity potential $\tilde{\phi}$ is converted into water velocity $\mathbf{u}_\alpha$, where $\mathbf{u}_\alpha(x,y,t)=\nabla\phi(x,y,z_\alpha,t)$. The $O(\mu^2)$-model equations are written as

$$\frac{H_t}{\varepsilon} + \nabla\cdot(H\mathbf{u}_\alpha) + \mu^2\nabla\cdot\left\{H\left[\frac{z_\alpha^2}{2} - \frac{1}{6}(\varepsilon^2\zeta^2 - \varepsilon\zeta h + h^2)\right]\nabla S_\alpha + H\left[z_\alpha - \frac{1}{2}(\varepsilon\zeta - h)\right]\nabla T_\alpha\right\} = O(\mu^4) \tag{10}$$

$$\mathbf{u}_{\alpha t} + \varepsilon(\mathbf{u}_\alpha\cdot\nabla)\mathbf{u}_\alpha + \nabla\zeta + \mu^2\left\{\frac{1}{2}z_\alpha^2\nabla S_\alpha + z_\alpha\nabla T_\alpha\right\}_t + \varepsilon\mu^2\nabla\left\{\frac{1}{2}z_\alpha^2\mathbf{u}_\alpha\cdot\nabla S_\alpha + z_\alpha\mathbf{u}_\alpha\cdot\nabla T_\alpha + \frac{1}{2}T_\alpha^2 - \zeta T_{\alpha t}\right\} + \varepsilon^2\mu^2\nabla\left\{-\frac{\zeta^2}{2}S_{\alpha t} - \zeta\mathbf{u}_\alpha\cdot\nabla T_\alpha + \zeta S_\alpha T_\alpha\right\} + \varepsilon^3\mu^2\nabla\left\{\frac{\zeta^2}{2}(S_\alpha^2 - \mathbf{u}_\alpha\cdot\nabla S_\alpha)\right\} = O(\mu^4) \tag{11}$$

where $S_\alpha=\nabla\cdot\mathbf{u}_\alpha$ and $T_\alpha=\nabla\cdot(h\mathbf{u}_\alpha)+h_t/\varepsilon$.

Eqs. (8) and (9) can also be reduced to the Boussinesq's equations of Wu (1981), which assumed $O(\varepsilon)=O(\mu^2)$ and kept the terms up to $O(\varepsilon^2,\varepsilon\mu^2,\mu^4)$. The Boussinesq's equations read as

$$\frac{H_t}{\varepsilon} + \nabla\cdot(H\nabla\bar{\phi}) - \mu^2\nabla\cdot\left\{\left\{\frac{h}{2}[h_t + \nabla\cdot(h\nabla\bar{\phi})] - \frac{1}{3}h^2\nabla^2\bar{\phi}\right\}\nabla h\right\} = O(\varepsilon^2,\varepsilon\mu^2,\mu^4) \tag{12}$$

$$\bar{\phi}_t + \frac{1}{2}\varepsilon(\nabla\bar{\phi})^2 + \zeta - \mu^2\left\{\frac{h}{2}[h_t + \nabla\cdot(h\nabla\bar{\phi})]_t - \frac{1}{6}h^2\nabla^2\bar{\phi}_t\right\} = O(\varepsilon^2,\varepsilon\mu^2,\mu^4) \tag{13}$$

where $\bar{\phi}$=depth-averaged velocity potential, $\bar{\phi}=1/H\int_{-h}^{\varepsilon\zeta}\phi dz$.

For the recent decade, there have been developed several higher-order depth-integrated models for wave generation and propagation. Besides validating each higher-order model alone, it is also desired to examine how much improvement a higher-order model can actually make in predicting wave elevation and fluid velocity when compared with the lower-order models. In addition, since the higher-order models are much more complex mathematically, it is also of importance to examine the computational efficiency of these models, as well as to investigate whether the introduction of higher-order derivative terms can bring computational challenges in numerical simulations. A comparative study of the present fourth-order model and the two lower-order models Eqs. (10) and (11) and Eqs. (12) and (13) is another objective of the present study.

Numerical Algorithm

We note that the nondimensional Eqs. (8) and (9) include parameters ε and μ^2. It is desirable to rescale the equations so that these two parameters will no longer appear in the equations explicitly. The rescaling is for computational convenience and it will not change the properties of the equations. In the present study, we rescale the equations with the following factors:

$$(x,y,z,\zeta) = \frac{(x',y',z',\zeta')}{L_s},\quad t=\sqrt{\frac{g}{L_s}}t',\quad \phi=\frac{\phi'}{\varepsilon L_s\sqrt{gL_s}} \tag{14}$$

where L_s=length of the landslide.

It is observed in the present study that the stability of the numerical model can be improved significantly by regrouping the integrated momentum in Eq. (9), namely, by letting all the time derivatives of $\tilde{\phi}$ be kept on the left-hand side as

$$U_t = -F_b \tag{15}$$

where

$$U = \tilde{\phi} + (Ah - H)F_1 + (Bh^2 - H^2)F_2 + (Ah - H)F_3 + (Bh^2 - H^2)F_4 + (Ch^3 - H^3)F_5 + (Dh^4 - H^4)F_6$$

$$F_b = \zeta + p + \frac{1}{2}\tilde{\phi}_x^2 + (F_1 + 2HF_2 + F_3 + 2HF_4 + 3H^2F_5 + 4H^3F_6)\zeta_t + \tilde{\phi}_x\Gamma_2 + \frac{1}{2}J_2^2 + \frac{1}{2}\Gamma_2^2 + \tilde{\phi}_x\Gamma_4 + J_2J_4$$

In the following, the finite-difference algorithm constructed in this study is described for one-dimensional cases. The details of present algorithm are presented in Appendix. The time integration is approximated with the higher-order Adams-Bashforth-Moulton predictor-corrector scheme, which includes a fifth-order predictor and a sixth-order corrector stages and is similar to that of Gobbi and Kirby (1999). Both Eqs. (8) and (15) include first-order time derivatives, such as h_t, $\tilde{\phi}_t$, and ζ_t. In the present study, these terms are computed with fourth-order accuracy in the predictor stage and fifth-order accuracy in the corrector stage. The computational domain is discretized with uniform grids. The coordinates of grid nodes are denoted as $x_i=(i-1)\Delta x$, where $i=1,2,\ldots,N$ are the indices. For a given variable such as $\tilde{\phi}$, the spatial derivatives on an internal grid node, i.e., $i=4,5,\ldots,N-2$, are approximated through the central difference scheme within seven-point stencil. By assuming fully reflective boundary, we introduce image nodes outside the computational domain. Quantities of variables on these image nodes are determined based on the internal nodes. For example, on an image node $(i=-1)$ neighboring the boundary node $(i=1)$, the value of a vector variable can be determined as $(\tilde{\phi}_x)_{-1}=-(\tilde{\phi}_x)_2$, and the value of a scalar variable is $\tilde{\phi}_{-1}=\tilde{\phi}_2$. As a result, the central difference schemes Eqs. (33)–(36) are also applied to the boundary nodes $i=1,2,3$ and $i=N-2,N-1,N$. In the discretized form, Eq. (15) yields a set of linear algebraic equations with a diagonal coefficient matrix of bandwidth of seven. Note that the nonlinear and weakly dispersive terms in the governing equations only include first- and second-order spatial derivatives. As a result, the present finite difference scheme is accurate to an order of $O(\Delta x^6)$ in $O(1)$ and $O(\mu^2)$ terms, and has truncation errors of $O(\Delta x^4)$ in the higher-order dispersive terms of $O(\mu^4)$.

The present model equations include spatial and time derivatives of water depth up to fourth-order. These higher-order terms may become singular at a node where water depth varies, and introduce high-frequency noises to the simulation results. To improve the numerical stability, in this study, we employ the sixth-order Savitzky-Golay smoothing filter to ζ and $\tilde{\phi}$ once every 50 time steps, and to the second- and higher-order derivatives of h at each time step. The same numerical algorithm is also applied to lower-order models by Wu (1981) and Lynett and Liu (2002).

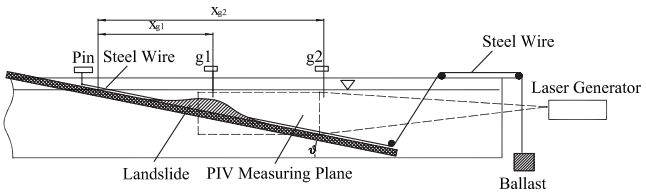

Fig. 2. Sketch of the experimental setup and the definition of the main parameters

Laboratory Experiments

As mentioned earlier, experimental results which are applicable to validate depth-integrated models are relatively scarce. Experimental data on fluid velocities induced by landslide models are even rarer. In the present study, we perform a series of wave flume experiments to measure both the wave height and the water velocity generated by different landslide models sliding down on inclines with different slopes. In this paper, due to the page limit, we present the results from two sets of the experiments, which are referred to as cases A and B.

A sketch of the experimental configuration is shown in Fig. 2. The experiments are conducted in a wave flume in the hydraulics laboratory of the Department of Civil and Environmental Engineering at the University of Hawaii. The wave flume is quite narrow and suitable for one-dimensional studies. The specific dimensions of the flume are 0.152 m (6 in.) wide, 0.406 m (16 in.) deep, and 9.754 m (32 ft) long. The bottom and side walls are mostly constructed with Plexiglas. One side wall in the middle section is made with glass to enhance the light transmission for particle image velocimetry (PIV). Installed in the middle section is an artificial incline made of a Plexiglas plate and painted black to absorb incoming laser light. Other important parameters associated with the experiments include the angle θ of the incline along which the landslide model slides down in water, and the initial submergence depth of the landslide model h_{0c}, which is the depth measured above the midpoint of the landslide model at its initial position. We install two resistance-type wave gauges, "g1" and "g2," to pick up the time series of water surface elevations. The locations of the wave gauges are denoted as x_{g1} and x_{g2}, and the local water depth at the two gauge locations are h_1 and h_2, respectively. In the experiments, wave gauge g1 is always above the midpoint of the landslide model before it is released to slide. The specific values for these parameters in the experimental cases A and B are presented in Table 1.

In Case A and Case B of the experimental study, the landslide model is made of aluminum. A photo of the model is shown in Fig. 3. The model has a uniform cross-sectional area over the width. The top surface of the model follows a truncated cosine function

Table 1. Configuration of Landslide Experiments

Case #	θ (degrees)	h_{0c} (m)	x_{g1} (m)	x_{g2} (m)	h_1 (m)	h_2 (m)
A	10	0.090	0.618	1.128	0.109	0.199
B	15	0.045	0.251	0.792	0.065	0.205

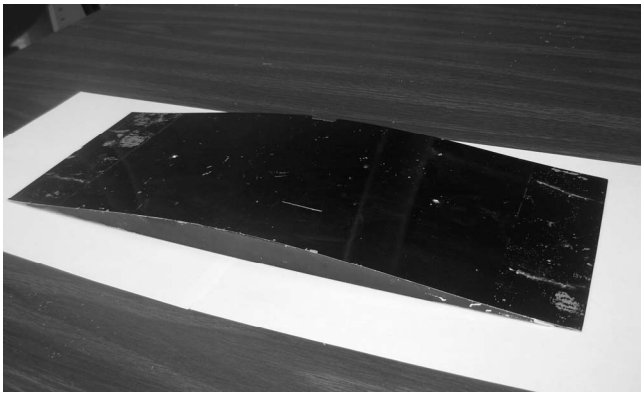

Fig. 3. Landslide model used in the experiments

$$b(x) = \frac{b_m}{2}\left[1 + \cos\left(\frac{2\pi}{L_0}x\right)\right], \quad \text{for} \quad -L_m/2 \leq x \leq L_m/2 \quad (16)$$

where b_m=0.019 m (0.75 in.)=maximum height; L_m=0.394 m (15.5 in.)=length of model; and L_0=0.457 m (18 in.)=projected length of the full-period cosine curve. Due to the truncated shape of the landslide model, the water depth is discontinuous over the front and rear tips. This may cause singularity in the higher-order derivatives of water depth. In the present study, we modify the landslide geometry in the numerical simulations such that it has the same volume as the prototype but a full-period cosine shape. The length of the modified landslide geometry is L_s=0.455 m, determined by the following equation:

$$\frac{b_m}{2}\int_{-L_s/2}^{L_s/2}\left[1 + \cos\left(\frac{2\pi}{L_s}x\right)\right]dx = \frac{b_m}{2}\int_{-L_m/2}^{L_m/2}\left[1 + \cos\left(\frac{2\pi}{L_0}x\right)\right]dx \quad (17)$$

A sketch of the cross section of the landslide model is presented in Fig. 4.

In the experiments, a pulley system is used to drive the model sliding down the artificial incline. Initially, the landslide model is held on the incline by a pin. We install an electronic switch and connect it to the pin. This enables us to record the time when the pin is raised up and the model starts sliding.

The velocities of water particles are measured by a PIV system from TSI, Inc. This system includes a dual Nd:YAG laser generator, laser sheet optics which converts the laser beam into a laser sheet, a high-speed video camera, a laser pulse synchronizer, and the PIV processing software Insight 3G. The laser generator has two laser heads. In the present experiments, each laser head emits a laser pulse of 120 mJ at a frequency of 29 Hz, which is also the sampling frequency of PIV. The laser sheet is shot into the water flume from the downstream end of the flume to illuminate the vertical two-dimensional PIV measuring plane above the artificial incline. For each measurement, the video camera captures a pair

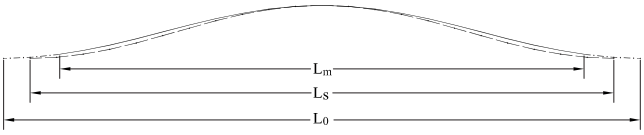

Fig. 4. Cross-sectional geometry of the landslide model: actual top surface (solid); the modified full-period cosine shape (dash); and the prototype full-period cosine shape (dashed-dot)

Table 2. Experimental Measurements

Case #	a_s (m/s)	t_s (s)	$\max(\lvert\zeta/h_1\rvert)$	$\max(\lvert\zeta/h_2\rvert)$
A	2.131	0.72	0.036	0.056
B	2.419	0.56	0.065	0.049

of images with a time interval of 6,000 μs. The images are then saved into the computer and processed to obtain the instantaneous water velocity fields. To record the flow dynamics during the entire travel of the landslide model, for each run of the experiment, a total of 200 PIV captures are made continuously.

Each experimental case is repeated for more than five times. The repeatability of the experiment is investigated by comparing the time series of landslide displacements and water surface elevations. It is found that the results from different runs are very consistent. In this paper, we present the representative results from a typical run in each of the experimental cases.

In Table 2, we present the maximum water surface displacements measured in both experiments. These results have been converted into nondimensional form based on the local water depths h_1 and h_2 at the two gauge locations, respectively. The other parameters in Table 2 describe the landslide motion. The displacement of the landslide model is read from the raw images taken by the PIV camera. In both experiments, we observe that the landslide model has nearly a constant acceleration along the slope after a very brief initial adjusting period and before reaching the bottom of the slope. Therefore, the displacements can be predicted by a quadratic function of time, i.e.

$$s = \frac{a_s t^2}{2}, \quad \text{for} \quad t \leq t_s \quad (18)$$

where s=displacement of the landslide model; a_s=acceleration; and t_s denotes the total time period of landslide motion. The comparisons between the measured and predicted displacements are plotted in Fig. 5 which shows an excellent agreement between the two.

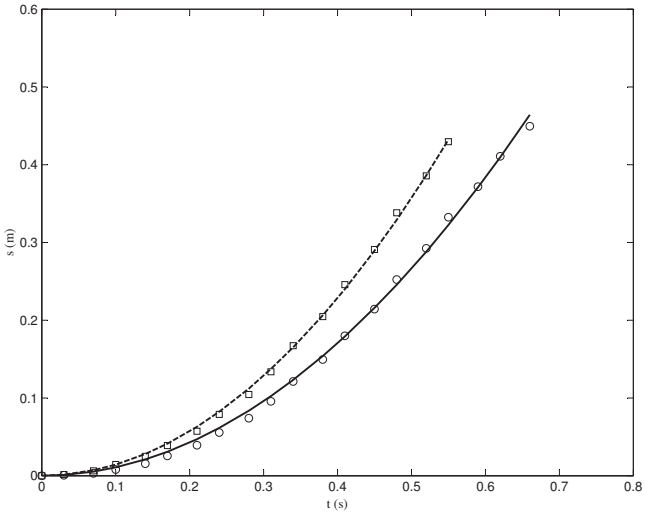

Fig. 5. Displacements of the landslide model: the predicted (Case A: solid; Case B: dashed) and the measured in the experiment (Case A: circle; Case B: square)

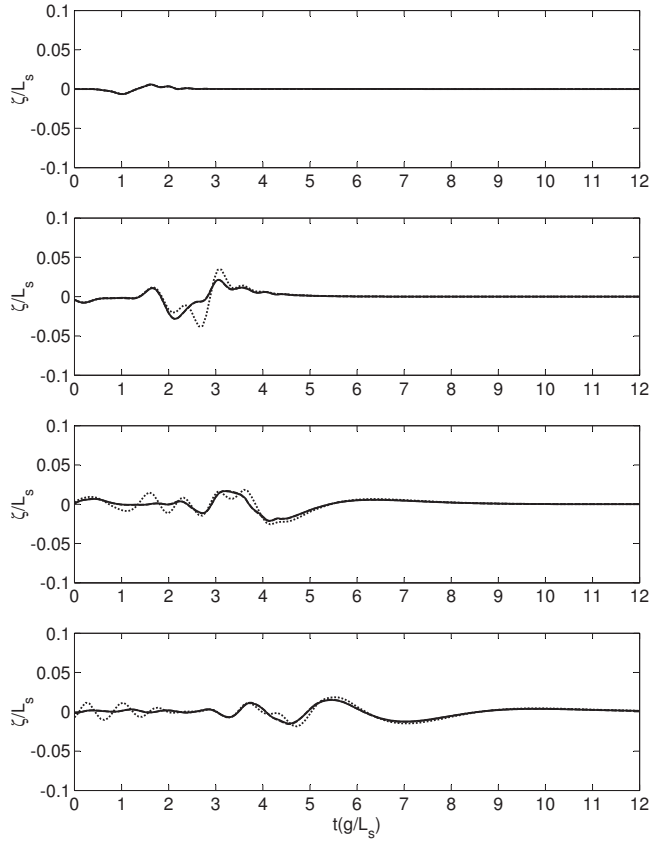

Fig. 6. Test on numerical convergence: water surface profiles simulated with the present $O(\mu^4)$-model: $\Delta x/L_s=0.02$ (solid); 0.04 (dashed); 0.08 (dot)

Validation of Numerical Models

In this study, we numerically simulate the experiments with the present $O(\mu^4)$-model, as well as $O(\mu^2)$-model by Lynett and Liu (2002) and Boussinesq model by Wu (1981) for comparison and validation. Instead of tracking the runup and drawdown of waterlines along the slope at the upstream end, we assume the slope is always fully submerged, starting upstream from a shallow water channel with a tiny constant water depth of 0.02 L_s, as illustrated in Fig. 1. The computational domain has a fixed length and is bounded by vertical walls on the upstream and downstream ends. The vertical walls are set sufficiently far away from the wave-generation source so that the simulations are not contaminated by the reflected waves.

In a finite-difference scheme, computational accuracy can be affected by the grid sizes applied to discretize the computational domain. Tests on numerical convergence need to be performed before the numerical model is applied. In the present study, the numerical convergence and computational efficiency of the present $O(\mu^4)$-model are investigated based on the experimental Case A. We discretize the one-dimensional domain with grid sizes of 0.02 L_s, 0.04 L_s, and 0.08 L_s, respectively, and employ a constant time step of 0.001 $\sqrt{L_s/g}$. The numerical model is run for 12,000 dimensionless time steps. Fig. 6 shows the simulated water surface profiles. Comparisons of the simulated wave elevations among different grid sizes indicate a trend of convergence as the grid sizes decrease and very good consistence between the simulations with grid sizes of 0.02 L_s and 0.04 L_s. To quantify this comparison, we compute the determination coefficients, R^2, for

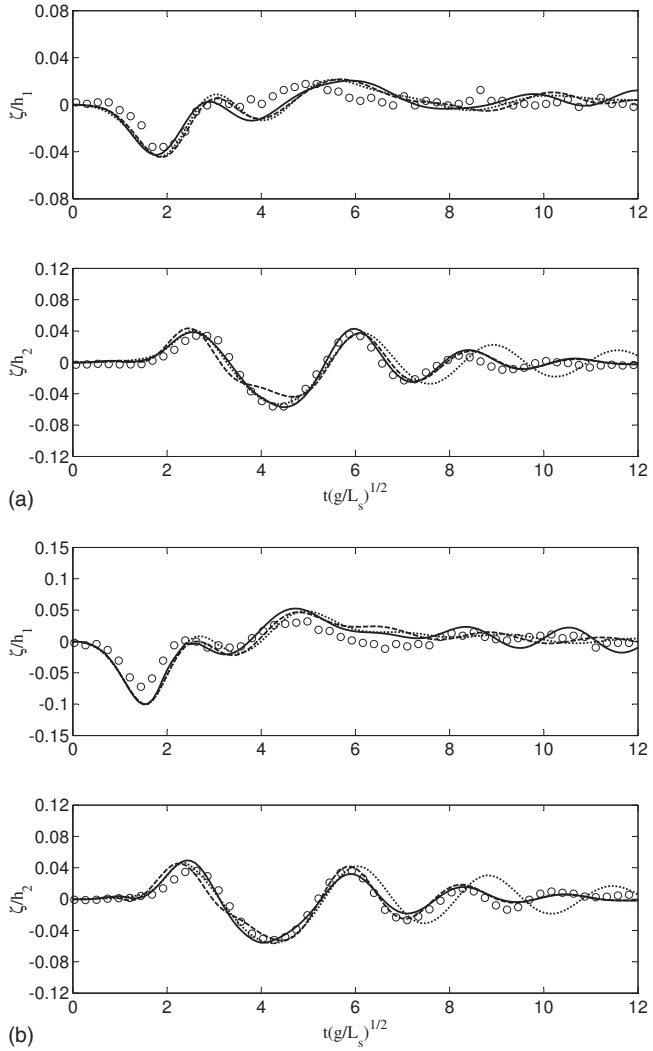

Fig. 7. Time series of water surface displacements measured by wave gauge "g1" (top) and by wave gauge "g2" (bottom), with the results based on the present $O(\mu^4)$-model (solid), the $O(\mu^2)$-model (dashed), the Boussinesq model (dot), and experiments (circle): (a) Case A; (b) Case B

simulated surface profiles at $t\sqrt{g/L_s}=12$, and yield $R^2=0.7137$ between 0.04 L_s and 0.08 L_s, and $R^2=0.9976$ between 0.02 L_s and 0.04 L_s. Numerical convergence of the other two models is also investigated with the same grid sizes, and shows very good consistence between grid sizes of 0.02 L_s and 0.04 L_s as well.

In this study, numerical simulations of both experimental cases A and B are performed with a uniform grid size of 0.04 L_s and a constant time step of 0.001 $\sqrt{L_s/g}$ for all the three wave models. Plotted in Fig. 7 are the time series of water surface displacements measured in the experiments and simulated by the numerical models. The water surface displacements are presented in nondimensional forms based on the local water depths h_1 and h_2, respectively. The waves measured by wave gauge g1 in the near field show that the landslide model first generates a depression. Then the water surface bounces up to develop a trailing peak. The far-field waves at wave gauge g2 include a leading wave of relatively long wavelength, which is followed by a train of oscillatory waves of quickly decaying wave amplitude. These figures show that for waves measured at the location of wave gauge g1, the waves are not fully developed yet as the location is very close to

Table 3. Determination Coefficients (R^2) for the Numerical Simulations

Case #	Boussinesq model	$O(\mu^2)$-model	$O(\mu^4)$-model
A	0.750	0.811	0.931
B	0.510	0.848	0.890

the initial unperturbed location of the landslide model. In this situation, all three models seem to predict quite similar results for the wave height. At the location of wave gauge g2, the waves are fully developed and the dispersive effect became very apparent. When we examine the trailing oscillatory waves, the present $O(\mu^4)$-model and the $O(\mu^2)$-model provide much better agreement with the experiments on wave frequency than the standard Boussinesq model. For wave amplitude, the present new $O(\mu^4)$-model gives the most accurate prediction. To further quantify the comparisons, we also calculate R^2 for all the numerical simulations based on the far-field waves at wave gauge g2. The computed R^2 values are listed in Table 3. The comparisons clearly indicate that the new $O(\mu^4)$-model provides the best agreement with both experimental cases.

In Fig. 8, we plot the velocity profiles simulated by the three numerical models and measured in the experimental Case B at two representative time instants. In the experiments, the PIV measurement window is fixed at one location. After the landslide model is released from the upstream, it slides down along the incline, and passes through the measurement window. The waves also pass through the same window during their different stages of development. The results presented in Fig. 8 are measured at two different time instants. The first one, i.e., Stage (a), is when the landslide model just enters the measurement window and the velocity profile is calculated for a vertical section located ahead of the model, as shown in Fig. 8(a). The second stage, namely, Stage (b), is when the model is exiting from the measurement window, and the velocity profile is calculated for a vertical section behind the model where the shorter trailing waves are developed, as shown in Fig. 8(b). In Fig. 8, the magnitudes of the water velocities are normalized based on the local water depth h_l=0.168 m on the section. In this figure, u is the horizontal velocity while w denotes the vertical velocity. In Stage (a), both the horizontal and vertical components of the water velocities have very low magnitudes. The gradients of water velocities are also very small along the water depth. All the three numerical models have a reasonably good agreement with the experiment. Under the shorter waves in Stage (b), the vertical water velocity w has a higher gradient along the water depth, for which only the $O(\mu^4)$-model yields good prediction. The quadratic approximation of the water velocity profiles in the lower-order Boussinesq models becomes insufficient in this case. In Figs. 9 and 10, we plot the time series of water velocities at five fixed points along the chosen vertical section. The $O(\mu^4)$-model is seen to predict the water velocities with excellent accuracy.

Besides the validation results presented in this paper, additional comparisons between the present fourth-order model and other experimental cases have also been carried out. For example, the comparison between the present model and the experimental results from Hammack (1973) on waves generated by an impulsive bed upthrust showed excellent agreement. These additional results can be found in Zhou (2008) and Zhou and Teng (2009).

All the results indicate that the new $O(\mu^4)$-model has the best prediction for both water waves and water velocities. The $O(\mu^2)$-model by Lynett and Liu (2002) is also accurate for most situations. We would like to point out that in the present study, the cases being investigated involved relatively long disturbances and mild slopes of the incline. While these may simulate most of the situations in the real oceans, we recognize that there are cases where the length of the landslide can be short and the slope where a land mass fails can also be steep. It will be valuable to conduct further numerical and experimental studies to examine the validity of various wave models for cases with short landslide and steep slopes. In addition, we should mention that even though the new $O(\mu^4)$-model provides the best prediction for both the water wave and the fluid velocity, the difference between the new model

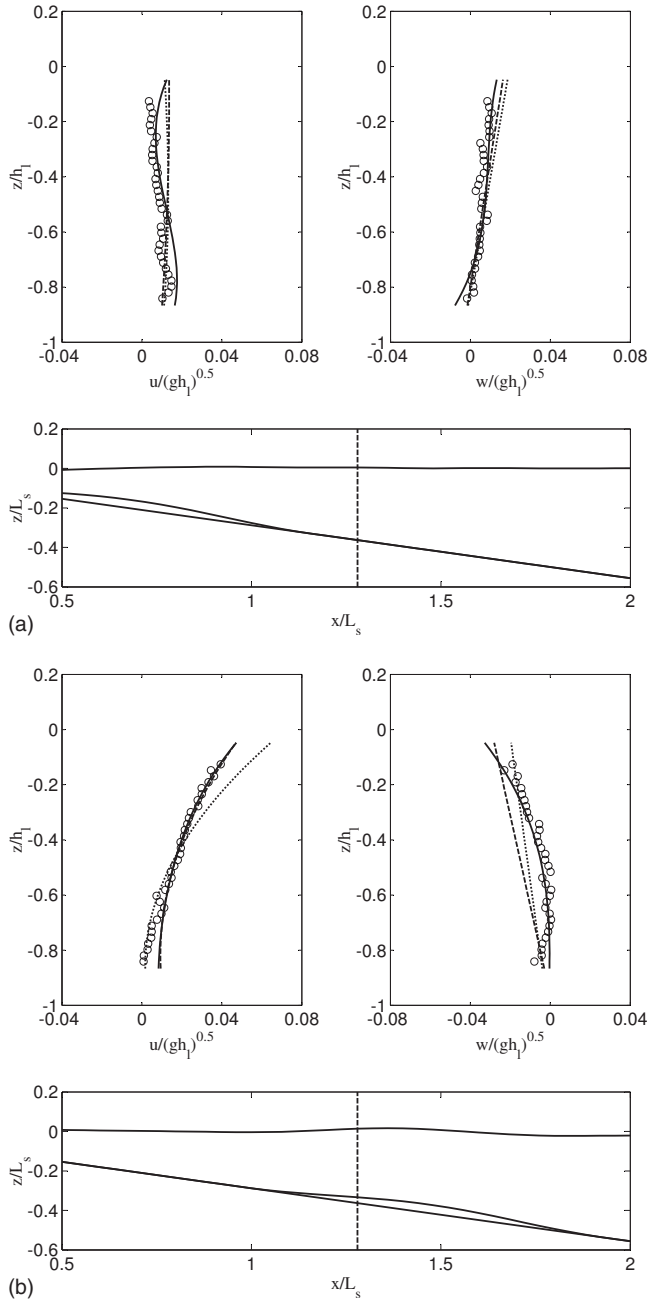

Fig. 8. Water velocity profiles in Case B: the $O(\mu^4)$-model (solid); the $O(\mu^2)$-model (dashed); the Boussinesq model (dot); and experiment (circle). The bottom plot sketches the landslide and wave profiles simulated by the present $O(\mu^4)$-model. Dashed line indicates the section on which the velocity profiles are obtained: (a) $t\sqrt{g/L_s}$=0.9; (b) $t\sqrt{g/L_s}$=5.1.

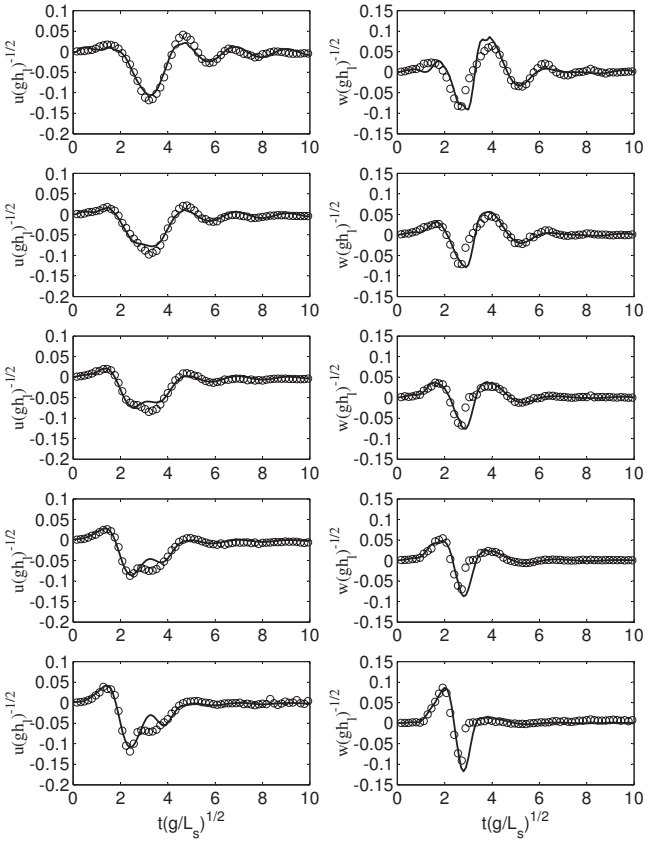

Fig. 9. Time series of water velocities in Case A: the present $O(\mu^4)$-model (solid) and the experiment (circle). From top to bottom: z/h_l =−0.131, −0.311, −0.492, −0.678, and −0.852. Local water depth is h_l=0.161 m.

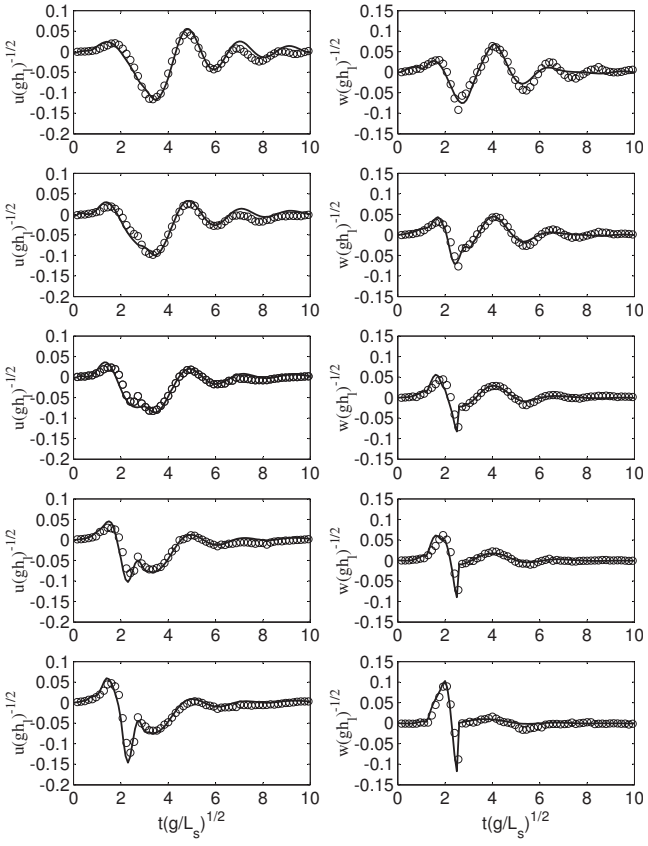

Fig. 10. Time series of water velocities in Case B: the present $O(\mu^4)$-model (solid) and the experiment (circle). From top to bottom: z/h_l=−0.126, −0.300, −0.473, −0.646, and −0.820. Local water depth is h_l=0.168 m.

and the existing lower-order models is not critical. In fact, the higher-order derivative terms in the higher-order models often generate high-frequency noises and cause numerical instability in the simulations. Using filtering techniques can help smooth out the numerical noises. However, if used incorrectly, the filters can also alter the numerical results and introduce errors. Therefore, for engineering applications, if our main concern is the computational efficiency then the lower-order models may still be used and considered as quite acceptable.

We would also like to mention that in the present model, the shape and motion of the landslide are considered as a given input to the wave equations. The present wave model does not predict the evolution of the landslide itself. Even though the landslide models used in our experiments are rigid, the present wave model is applicable to deformable landslides as long as the evolution of the landslide is known and can be prescribed as an input to the wave model.

Conclusions

In this study, the fully nonlinear fourth-order dispersive model for wave propagation by Gobbi and Kirby (1999) is extended so that it can also be applied to predict the wave generation by submerged moving disturbances. A higher-order finite-difference scheme is constructed to solve the equations. The new model is validated against two sets of laboratory experiments on landslide-generated waves conducted in this study. In the experiments, the time series of water surface displacements as well as the water velocities are measured with resistance-type wave gauges and PIV, respectively. The experiments are then simulated numerically with the present higher-order model and two existing weakly dispersive models. Comparisons between the experiments and the numerical models indicate that the new higher-order model has clear improvement over the lower-order ones, due to the higher-order dispersive terms and the fourth-order approximation of the velocity distribution along the water depth. This study is among the first to measure fluid velocities induced by landslide models in a wave flume and to validate a higher-order depth-integrated model for both surface wave and the water velocity. The experimental data can be useful to other researchers to validate their wave models in the future.

Acknowledgments

The present study was partially funded by the National Science Foundation in the form of a graduate research assistantship, and the U.S. National Research Council of National Academies through a research associateship for postdoctoral researchers. The laboratory experiments have also received support from the College of Engineering and the Graduate Student Organization of the University of Hawaii. The writers thank Dr. In Mei Sou, Mr. Richard Carter, and Mr. Ravi Mohandie for their assistance in the laboratory experiments. Helpful discussions with Professor Philip Liu of Cornell University, Professor James Kirby of the

University of Delaware, and Professor Patrick Lynett of the Texas A&M University on the general concepts of higher-order wave modeling are also gratefully acknowledged.

Appendix. Numerical Scheme

Let the model equations be represented as $y_t=f(y,t)$. The predictor stage reads

$$y_p^{n+1}=y^n+\frac{\Delta t}{720}(1{,}901f^n-2{,}774f^{n-1}+2{,}616f^{n-2}-1{,}274f^{n-3}+251f^{n-4})+O(\Delta t^6) \tag{19}$$

where the subscript "p" denotes the predicted value, and "n" denotes the present time level. The sixth-order implicit corrector stage is written as

$$y^{n+1}=y^n+\frac{\Delta t}{1{,}440}(475f_p^{n+1}+1{,}427f^n-798f^{n-1}+482f^{n-2}-173f^{n-3}+27f^{n-4})+O(\Delta t^7) \tag{20}$$

The corrector stage requires iteration until a convergence criterion is reached. In the present study, we set

$$\frac{\sum_{i=1}^{N}|\tilde{\phi}_i^{n+1}-\tilde{\phi}_{i,*}^{n+1}|}{\sum_{i=1}^{N}|\tilde{\phi}_i^{n+1}|}+\frac{\sum_{i=1}^{N}|\zeta_i^{n+1}-\zeta_{i,*}^{n+1}|}{\sum_{i=1}^{N}|\zeta_i^{n+1}|}<10^{-6} \tag{21}$$

in which * denotes the value computed in the previous iteration.

The formulas employed in the predictor stage for $\tilde{\phi}_t$ read

$$\tilde{\phi}_t^{n-4}=\frac{1}{12\Delta t}(-3\tilde{\phi}^n+16\tilde{\phi}^{n-1}-36\tilde{\phi}^{n-2}+48\tilde{\phi}^{n-3}-25\tilde{\phi}^{n-4})+O(\Delta t^4) \tag{22}$$

$$\tilde{\phi}_t^{n-3}=\frac{1}{12\Delta t}(\tilde{\phi}^n-6\tilde{\phi}^{n-1}+18\tilde{\phi}^{n-2}-10\tilde{\phi}^{n-3}-3\tilde{\phi}^{n-4})+O(\Delta t^4) \tag{23}$$

$$\tilde{\phi}_t^{n-2}=\frac{1}{12\Delta t}(-\tilde{\phi}^n+8\tilde{\phi}^{n-1}-8\tilde{\phi}^{n-3}+\tilde{\phi}^{n-4})+O(\Delta t^4) \tag{24}$$

$$\tilde{\phi}_t^{n-1}=\frac{1}{12\Delta t}(3\tilde{\phi}^n+10\tilde{\phi}^{n-1}-18\tilde{\phi}^{n-2}+6\tilde{\phi}^{n-3}-\tilde{\phi}^{n-4})+O(\Delta t^4) \tag{25}$$

$$\tilde{\phi}_t^{n}=\frac{1}{12\Delta t}(25\tilde{\phi}^n-48\tilde{\phi}^{n-1}+36\tilde{\phi}^{n-2}-16\tilde{\phi}^{n-3}+3\tilde{\phi}^{n-4})+O(\Delta t^4) \tag{26}$$

In the corrector stage, the time derivatives are approximated by the following formulas:

$$\tilde{\phi}_t^{n-4}=\frac{1}{60\Delta t}(12\tilde{\phi}^{n+1}-75\tilde{\phi}^n+200\tilde{\phi}^{n-1}-300\tilde{\phi}^{n-2}+300\tilde{\phi}^{n-3}-137\tilde{\phi}^{n-4})+O(\Delta t^5) \tag{27}$$

$$\tilde{\phi}_t^{n-3}=\frac{1}{60\Delta t}(-3\tilde{\phi}^{n+1}+20\tilde{\phi}^n-60\tilde{\phi}^{n-1}+120\tilde{\phi}^{n-2}-65\tilde{\phi}^{n-3}-12\tilde{\phi}^{n-4})+O(\Delta t^5) \tag{28}$$

$$\tilde{\phi}_t^{n-2}=\frac{1}{60\Delta t}(2\tilde{\phi}^{n+1}-15\tilde{\phi}^n+60\tilde{\phi}^{n-1}-20\tilde{\phi}^{n-2}-30\tilde{\phi}^{n-3}+3\tilde{\phi}^{n-4})+O(\Delta t^5) \tag{29}$$

$$\tilde{\phi}_t^{n-1}=\frac{1}{60\Delta t}(-3\tilde{\phi}^{n+1}+30\tilde{\phi}^n+20\tilde{\phi}^{n-1}-60\tilde{\phi}^{n-2}+15\tilde{\phi}^{n-3}-2\tilde{\phi}^{n-4})+O(\Delta t^5) \tag{30}$$

$$\tilde{\phi}_t^{n}=\frac{1}{60\Delta t}(12\tilde{\phi}^{n+1}+65\tilde{\phi}^n-120\tilde{\phi}^{n-1}+60\tilde{\phi}^{n-2}-20\tilde{\phi}^{n-3}+3\tilde{\phi}^{n-4})+O(\Delta t^5) \tag{31}$$

$$\tilde{\phi}_t^{n+1}=\frac{1}{60\Delta t}(137\tilde{\phi}^{n+1}-300\tilde{\phi}^n+300\tilde{\phi}^{n-1}-200\tilde{\phi}^{n-2}+75\tilde{\phi}^{n-3}-12\tilde{\phi}^{n-4})+O(\Delta t^5) \tag{32}$$

For a given variable such as $\tilde{\phi}$, the spatial derivatives on an internal grid node, i.e., $i=4,5,\ldots,N-3$, are approximated through the central difference scheme within seven-point stencil

$$(\tilde{\phi}_i)_x=\frac{1}{60\Delta x}(-\tilde{\phi}_{i-3}+9\tilde{\phi}_{i-2}-45\tilde{\phi}_{i-1}+45\tilde{\phi}_{i+1}-9\tilde{\phi}_{i+2}+\tilde{\phi}_{i+3})+O(\Delta x^6) \tag{33}$$

$$(\tilde{\phi}_i)_{xx}=\frac{1}{180\Delta x^2}(2\tilde{\phi}_{i-3}-27\tilde{\phi}_{i-2}+270\tilde{\phi}_{i-1}-490\tilde{\phi}_i+270\tilde{\phi}_{i+1}-27\tilde{\phi}_{i+2}+2\tilde{\phi}_{i+3})+O(\Delta x^6) \tag{34}$$

$$(\tilde{\phi}_i)_{xxx}=\frac{1}{8\Delta x^3}(\tilde{\phi}_{i-3}-8\tilde{\phi}_{i-2}+13\tilde{\phi}_{i-1}-13\tilde{\phi}_{i+1}+8\tilde{\phi}_{i+2}-\tilde{\phi}_{i+3})+O(\Delta x^4) \tag{35}$$

$$(\tilde{\phi}_i)_{xxxx}=\frac{1}{6\Delta x^4}(-\tilde{\phi}_{i-3}+12\tilde{\phi}_{i-2}-39\tilde{\phi}_{i-1}+56\tilde{\phi}_i-39\tilde{\phi}_{i+1}+12\tilde{\phi}_{i+2}-\tilde{\phi}_{i+3})+O(\Delta x^4) \tag{36}$$

References

Agnon, Y., Madsen, P. A., and Schäffer, H. A. (1999). "A new approach to high-order Boussinesq models." *J. Fluid Mech.*, 399, 319–333.

Ataie-Ashtiani, B., and Najafi-Jilani, A. (2007). "A higher-order Boussinesq-type model with moving bottom boundary: Applications to submarine landslide tsunami waves." *Int. J. Numer. Methods Fluids*, 53, 1019–1048.

Chen, Q., Kirby, J. T., Dalrymple, R. A., Shi, F., and Thornton, E. B. (2003). "Boussinesq modeling of longshore currents." *J. Geophys. Res.*, 108(C11), 1–18.

Cruz, E. C., and Chen, Q. (2007). "Numerical modeling of nonlinear water waves over heterogeneous porous beds." *Ocean Eng.*, 34, 1303–1321.

Fine, I. V., Rabinovich, A. B., Bornhold, B. D., Thomson, R. E., and

Kulikov, E. A. (2005). "The Grand Banks landslide-generated tsunami of November 18, 1929: Preliminary analysis and numerical modeling." *Mar. Geol.*, 215, 45–57.
Fine, I. V., Rabinovich, A. B., Thomson, R. E., and Kulikov, E. A. (2003). "Numerical modeling of tsunami generation by submarine and subaerial landslides." *Submarine landslides and tsunamis*, A. C. Yalçiner, E. Pelinovsky, E. Okal, and C. E. Synolakis, eds., Kluwer Academic, Boston, 69–88.
Fuhrman, D. R., and Madsen, P. A. (2008). "Simulation of nonlinear wave run-up with a high-order Boussinesq model." *Coastal Eng.*, 55, 139–154.
Fuhrman, D. R., and Madsen, P. A. (2009). "Tsunami generation, propagation, and run-up with a high-order Boussinesq model." *Coastal Eng.*, 56, 747–758.
Geist, E. L., Lynett, P. J., and Chaytor, J. D. (2009). "Hydrodynamic modeling of tsunamis from the Currituck Landslide." *Mar. Geol.*, 264, 41–52.
Gobbi, M. F., and Kirby, J. T. (1999). "Wave evolution over submerged sills: Tests of a high-order Boussinesq model." *Coastal Eng.*, 37, 57–96.
Gobbi, M. F., Kirby, J. T., and Wei, G. (2000). "A fully nonlinear Boussinesq model for surface waves. Part 2. Extension to $O(kh)^2$." *J. Fluid Mech.*, 405, 181–210.
Grilli, S. T., Vogelmann, S., and Watts, P. (2002). "Development of a 3D numerical wave tank for modeling tsunami generation by underwater landslides." *Eng. Anal. Boundary. Elem.*, 26, 301–313.
Grilli, S. T., and Watts, P. (1999). "Modeling of waves generated by a moving submerged body: Applications to underwater landslides." *Eng. Anal. Boundary. Elem.*, 23, 645–656.
Grilli, S. T., and Watts, P. (2005). "Tsunami generation by submarine mass failure. I: Modeling experimental validation, and sensitivity analyses." *J. Waterway, Port, Coastal, Ocean Eng.*, 131(6), 283–297.
Hammack, J. L. (1973). "A note on tsunamis: Their generation and propagation in an ocean of uniform depth." *J. Fluid Mech.*, 60, 769–799.
Hampton, M. A., Lee, H. J., and Locat, J. (1996). "Submarine landslides." *Rev. Geophys.*, 34(1), 33–59.
Hsiao, S.-C., Liu, P. L.-F., and Chen, Y. (2002). "Nonlinear water waves propagating over a permeable bed." *Proc. R. Soc. London*, 458, 1291–1322.
Hsiao, S.-C., Lynett, P., Hwung, H.-H., and Liu, P. L.-F. (2005). "Numerical simulations of nonlinear short waves using a multiplayer model." *J. Eng. Mech.*, 131, 231–243.
Imran, J., Harff, P., and Parker, G. (2001). "A numerical model of submarine debris flow with graphical user interface." *Comput. Geosci.*, 27, 717–729.
Jiang, L., and LeBlond, P. H. (1992). "The coupling of a submarine slide and the surface water waves which it generates." *J. Geophys. Res.*, 97(C8), 12731–12744.
Jiang, L., and LeBlond, P. H. (1993). "Numerical modeling of an underwater Bingham plastic mudslide and the waves which it generates." *J. Geophys. Res.*, 98(C6), 10303–10317.
Liu, P. L.-F., Wu, T.-R., Raichlen, F., Synolakis, C. E., and Borrero, J. C. (2005). "Runup and rundown generated by three-dimensional sliding masses." *J. Fluid Mech.*, 536, 107–144.
Løvholt, F., Pedersen, G., and Gisler, G. (2008). "Oceanic propagation of a potential tsunami from the La Palma Island." *J. Geophys. Res.*, 113, C09026.
Lynett, P. J., and Liu, P. L.-F. (2002). "A numerical study of submarine-landslide-generated waves and run-up." *Proc. R. Soc. London*, 458, 2885–2910.
Lynett, P. J., and Liu, P. L.-F. (2004). "A two-layer approach to wave modelling." *Proc. R. Soc. London*, 460, 2637–2669.
Madsen, P. A., Bingham, H. B., and Liu, H. (2002). "A new Boussinesq method for fully nonlinear waves from shallow to deep water." *J. Fluid Mech.*, 462, 1–30.
Madsen, P. A., Bingham, H. B., and Schäffer, H. A. (2003). "Boussinesq-type formulations for fully nonlinear and extremely dispersive water waves: Derivation and analysis." *Proc. R. Soc. London*, 459, 1075–1104.
Madsen, P. A., Fuhrman, D. R., and Wang, B.-L. (2006). "A Boussinesq-type method for fully nonlinear waves interacting with a rapidly varying bathymetry." *Coastal Eng.*, 53, 487–504.
Madsen, P. A., Murray, R., and Sørensen, O. R. (1991). "A new form of Boussinesq equations with improved linear dispersion characteristics." *Coastal Eng.*, 15, 371–388.
Madsen, P. A., and Sørensen, O. R. (1992). "A new form of Boussinesq equations with improved linear dispersion characteristics. Part 2: A slowly-varying bathymetry." *Coastal Eng.*, 18, 183–204.
Nwogu, O. (1993). "Alternative form of Boussinesq equations for near-shore wave propagation." *J. Waterway, Port, Coastal, Ocean Eng.*, 119(6), 618–638.
Rabinovich, A. B., Thomson, R. E., Kulikov, E. A., Bornhold, B. D., and Fine, I. V. (1999). "The landslide-generated tsunami of November 3, 1994 in Skagway Harbor, Alaska: A case study." *Geophys. Res. Lett.*, 26(19), 3009–3012.
Schäffer, H. A., and Madsen, P. A. (1995). "Further enhancements of Boussinesq-type equations." *Coastal Eng.*, 26, 1–14.
Sue, L. P., Nokes, R. I., and Walters, R. A. (2006). "Experimental modeling of tsunami generated by underwater landslides." *Sci. Tsunami Hazards*, 24(4), 267–287.
Villeneuve, M., and Savage, S. B. (1993). "Nonlinear, dispersive, shallow-water waves developed by a moving bed." *J. Hydraul. Res.*, 31(2), 249–266.
Watts, P. (1998). "Wavemaker curves for tsunamis generated by underwater landslides." *J. Waterway, Port, Coastal, Ocean Eng.*, 124(3), 127–137.
Watts, P. (2000). "Tsunami features of solid block underwater landslides." *J. Waterway, Port, Coastal, Ocean Eng.*, 126(3), 144–152.
Wei, G., and Kirby, J. T. (1995). "A time-dependent numerical code for extended Boussinesq equations." *J. Waterway, Port, Coastal, Ocean Eng.*, 121, 251–261.
Wei, G., Kirby, J. T., Grilli, S. T., and Subramanya, R. (1995). "A fully nonlinear Boussinesq model for surface waves. Part 1. Highly nonlinear unsteady waves." *J. Fluid Mech.*, 294, 71–92.
Wiegel, R. L. (1955). "Laboratory studies of gravity waves generated by the movement of a submarine body." *Trans., Am. Geophys. Union*, 36(5), 759–774.
Wu, T. Y. (1981). "Long waves in ocean and coastal waters." *J. Eng. Mech.*, 107, 501–522.
Yuk, D., Yim, S. C., and Liu, P. L.-F. (2006). "Numerical modeling of submarine mass-movement generated waves using RANS model." *Comput. Geosci.*, 32, 927–935.
Zhou, H.-Q. (2008). "A higher-order depth-integrated model for water waves and currents generated by underwater landslides." Ph.D. dissertation, Univ. of Hawaii at Manoa, Honolulu.
Zhou, H.-Q., and Teng, M. H. (2009). "Higher order modeling of water waves generated by submerged moving disturbances." *Proc., 28th Int. Conf. on Ocean, Offshore and Arctic Engineering, OMAE-2009 Conf.*, Honolulu.